EVOLUTION OF ISOLATED TURBULENT TRAILING VORTICES

Karthik Duraisamy
Department of Aerospace Engineering,
University of Glasgow, Glasgow G12 8QQ, Scotland
dkarthik@eng.gla.ac.uk

Sanjiva K Lele
Department of Aeronautics and Astronautics and Mechanical Engineering,
Stanford University, Stanford 94305, CA, USA.
lele@stanford.edu

Abstract

In this work, the temporal evolution of a low swirl-number turbulent Batchelor vortex is studied using pseudo-spectral direct numerical simulations. The solution of the governing equations in the vorticity-velocity form allows for accurate application of boundary conditions. The physics of the evolution is investigated with an emphasis on the mechanisms that influence the transport of axial and angular momentum. Excitation of normal mode instabilities gives rise to coherent large scale helical structures inside the vortical core. The radial growth of these helical structures and the action of axial shear and differential rotation results in the creation of a polarized vortex layer. This vortex layer evolves into a series of hairpin-shaped structures that subsequently breakdown into elongated fine scale vortices. Ultimately, the radially outward propagation of these structures results in the relaxation of the flow towards a stable high-swirl configuration. Two conserved quantities, based on the deviation from the laminar solution, are derived and these prove to be useful in characterizing the polarized vortex layer and enhancing

the understanding of the transport process. The generation and evolution of the Reynolds stresses is also addressed.

1 Introduction

Coherent large scale vortices are present in many flows of physical and engineering interest such as tornadoes, airplane trailing vortices and swirling jets. Many such vortices are highly persistent, and therefore, the need to understand their evolution and decay is of considerable importance. In this work, the temporal evolution of an *isolated* turbulent Batchelor vortex is investigated. This flow is roughly representative of an airplane trailing vortex and is characterized by axisymmetric mean axial and azimuthal vorticity distributions given by qe^{-r^2} and re^{-r^2}, respectively. The swirl number q sets the relative magnitudes of the axial and azimuthal velocity distributions.

The temporal linear normal mode stability (using perturbations of the form $\boldsymbol{U}(r)e^{i(kx+m\theta-\omega t)}$, where k is the axial wavenumber, m is the azimuthal wavenumber and $\omega = \omega_r + i\omega_i$, with the real part representing the frequency and the imaginary part ω_i representing the growth rate) of this flow has been extensively studied ([1, 2, 3, 4, 5] etc.) and it is well recognized that strong inviscid helical instabilities are present for $q < 1.5$. These modes are unstable in the pure-jet condition ($q = 0$), present the highest growth levels near $q \approx 0.5$, and are ultimately stabilized for high swirl levels ($q \approx 1.5$). Stewartson and Brown [3] discovered a class of centre-modes, that lie very close to the neutral stability curve and are stabilized for $q > 2.31$. Heaton [4] shows that an infinite family of unstable centre-modes modes exist for $q < 2.31$. In the viscous case, unstable centre-modes have been shown to exist [5] at all swirl numbers. However, akin to the centre-modes in the inviscid case, the amplification rate of these modes are much smaller than that of the strong inviscid modes that prevail for $q < 1.5$. Transient growth of instabilities has been studied [6, 7], but appears to be important only in cases in which the normal mode instabilities are relatively weak. Spatial and spatio-temporal stability of this flow has also been studied [8, 9], but is not relevant to the current work since the focus is on the temporal evolution.

Turbulent evolution of a $q = 1.0$ Batchelor vortex has been studied using DNS and LES [10, 11, 12] and it has been established that while the helical normal mode instabilities play a dominant role in the early stages of the evolution, the non-linear interactions with the mean flow result in a saturation (during which the axial velocity has diminished significantly) and eventual decay. The initial swirl in this case is moderate enough to cause growth of the instabilities, but the relaxation to a stable high q configuration is very rapid. Delbende et al. [13] studied the non-linear evolution of single unstable helical modes over a range of swirl numbers and also

confirm the saturation of the growth rate. Further, they show that for $1 < q < 1.5$, the vortex ultimately relaxes towards an axisymmetric state. For lower values of swirl, it evolves into an array of smaller coherent vortices.

In this work, the temporal non-linear *and* turbulent evolution of a $q = 0.5$ Batchelor vortex is considered. The swirl number is in the range corresponding to the most amplified normal mode instabilities. High resolution pseudo-spectral DNS of the vorticity transport equations is performed along with an *accurate* treatment of the boundary conditions. The objective of the present study is to enhance the present understanding of the evolution process and to obtain physical insight into the mechanisms of turbulent transport of axial and angular momentum.

2 Methodology and problem set up

Many of the existing computational works (for instance, [10, 14]) on trailing vortices assume periodicity in the cross-stream directions. This means that the tangential velocity (and hence, the circulation) has to vanish at the boundaries, thus making the vortex unstable according to Rayleigh's centrifugal stability criteria [15]. In addition, an unphysical strain field will be set up by the image vortices. Pradeep et al. [16], demonstrate a computational case in which a trailing vortex is shown to be destabilized as a result of the application of transverse periodic boundary conditions. Alternately, Delbende et al. [13] decompose the velocity to a laminar part and a perturbation from the laminar solution and assume periodicity in the cross-stream direction for the perturbations. This can, however, potentially affect the solution of situations in which the pressure/velocity fluctuations can reach the boundary.

In the present work, the vorticity form of the incompressible Navier Stokes equations is solved using a pseudo-spectral approach. The rotational form of the vorticity transport equations is given by:

$$\frac{\partial \boldsymbol{\omega}}{\partial t} + \nabla \times (\boldsymbol{\omega} \times \mathbf{u}) = \nu \nabla^2 \boldsymbol{\omega} \tag{1}$$

The advantage of using these equations is that for a spatially compact distribution of the vorticity in the cross-flow direction, both the linear and non-linear terms are spatially compact, and hence, periodicity can be assumed. It has to be mentioned that this approach allows for non-periodic *irrotational* mean flow and perturbations at the boundary. A novel way of handling the boundary conditions in such an approach was proposed by Rennich and Lele [17]. This method is general and can be used for flows in which the vorticity is compact in the two unbounded dimensions and the third direction is periodic. In essence, the velocity $\boldsymbol{v}$

is decomposed into a vortical part and an irrotational part. At the cross-stream boundaries, where the vortical component is zero, the velocity is given by

$$\boldsymbol{v} = \nabla\phi + (A/2\pi r)\boldsymbol{e}_\theta + B\boldsymbol{e}_x, \tag{2}$$

where, A is the mean axial circulation and B ensures that the axial velocity in the potential region is zero. The velocity potential ϕ is obtained, in terms of Bessel functions, by employing a matching procedure along a cylindrical surface aligned with the longitudinal direction. The axial direction is assumed to be periodic. In addition to accurately representing the boundary conditions, this method proves to be highly efficient, since the boundaries of the computational domain can be close to the region of interest, *i.e.* commensurate with the compactness of the vorticity field. This methodology has been previously utilized in a related pilot work [18] to study the evolution of Batchelor vortices over a range of swirl numbers.

The initial base flow condition (v_θ is the tangential velocity and v_x is the axial velocity) is given by:

$$v_\theta = \frac{v_o\sqrt{\alpha}}{r}\left(1 - e^{-\alpha r^2}\right), \quad v_x = \frac{v_o}{q}e^{-\alpha r^2}, \tag{3}$$

where, $q = 0.5$ (highly unstable normal-mode configuration) and $v_o, 1/\sqrt{\alpha}$ are reference velocity and length scales, respectively. The Lamb's constant $\alpha = 1.25643$ is used such that the initial core-radius (identified as the radial location of peak v_θ) is $r_{co} = 1$. For all the plots, time is non-dimensionalized by the 'turnover time' $T = 2\pi v_o/r_{co}$. The Reynolds number (defined as $\Gamma/\nu = 2\pi v_o/\sqrt{\alpha}/\nu$) was set at 8000. A domain of size 40×15^2 was discretized on a mesh of dimension 512×192^2. The cross-stream dimension (15 times the original core-radius) was chosen based on the distance to which the vortical disturbances propagate within the temporal interval of interest. The axial dimension was selected such that the simulation could represent multiple periods of the most unstable normal mode (the wavelength of which roughly corresponds to 6 times the original core-radius). An isotropic turbulence field made compact in the cross-stream directions by a Gaussian function (further details in Appendix A) was added to the base flow on maturation. Runs with varying turbulence intensities and spectral content were performed and it was established that the qualitative features of the evolution remained similar as long as the initial intensity of the turbulence kinetic energy was less than roughly 2% of the mean flow kinetic energy. In this paper, a representative run of intensity 0.001% will be analyzed. This will be referred to as Case I (Isotropic). Turbulence and mean flow statistics are obtained by averaging in the axial and azimuthal directions.

To obtain a better qualitative understanding of various aspects of the evolution, a calculation, termed Case E (further details in Appendix B) starting from the most unstable Eigenfunction ($m = -2, k = 1$ from linear normal mode theory) will also be utilized. Case E is a helically symmetric flow[13].

3 Evolution

The temporal evolution of certain global quantities for Case I is shown in Fig. 1. As has been observed previously for a higher swirl number ($q = 1$) Batchelor vortex [10, 11], the turbulence kinetic energy shows a sharp growth phase followed by a saturation of the instabilities and eventual decay (Fig. 1a), gradually returning the vortex to a stable state. Spectral analysis revealed that most of the energy during the growth phase is concentrated in the most unstable normal mode (axial wavenumber ≈ 1 and azimuthal wave number ≈ -2), a fact that was also confirmed by flow visualization. For case E, the initial growth rate was found to match the results of the normal mode stability analysis (refer Appendix B). The peak axial velocity (and hence, the azimuthal vorticity) decays more rapidly than the peak azimuthal velocity (refer Fig. 1b, in which all the quantities are normalized by the value at t=0), resulting in a more stable configuration (or a higher q) at later times. Figure 1c shows that the core radius (radial location of peak tangential velocity) rapidly increases during the saturation phase. As will be seen later, this corresponds to a change in core structure. Also shown is the 'dispersion radius', which is qualitatively the edge of the turbulent region. This is quantitatively defined as the maximum radius at which the magnitude of the local vorticity $|\boldsymbol{\omega}| > 0.005|\boldsymbol{\omega}|_{max}$, where, $|\boldsymbol{\omega}|_{max}$ is the maximum vorticity in the spatial field. This is an important measure of the extent of momentum transfer and is seen to grow rapidly even during the decay phase.

During the growth phase, instability modes are excited inside the core and most of the energy of the turbulence is concentrated in the form of helical structures. These helical structures continue to grow and propagate radially outward, until the differential rotation that persists outside the core region acts to create azimuthally aligned fine-scale structures. Figure 2 shows an axial view of the instantaneous vorticity magnitude iso-surfaces during the decay phase. Outside the core, vorticity is filamented into fine-scale spirals that are predominantly aligned in the azimuthal direction. As will be seen from the plots of mean axial and azimuthal vorticity, the outermost ω_x structures are generally of a negative sense, and the corresponding ω_θ structures are of a positive sense. These fine scale structures are distinctly different from the largely

coherent motion inside the core and their radially outward advection is critical to the eventual stabilization of the core flow (their proximity is capable of exciting bending waves on the core structure as discussed in [19]) and transport of momentum to the exterior of the flow. The origin, characteristics and evolution of these structures will be investigated in detail in the following sections.

3.1 Evolution of single normal mode

The qualitative features of the turbulent evolution can be better understood if the evolution of a single normal mode (Case E) is considered (Figs. 3,4). In Case E, as the helical instability (an azimuthal '2' mode) grows, the alternating positive and negative 'lobes' of perturbation axial vorticity induce a radial velocity field that tends to distort the mean axial vorticity. Initially, the vorticity near the axis is distorted elliptically, with the major axis aligned with the positive perturbation lobes (Fig. 3b). Similar behavior is seen for the azimuthal vorticity (Fig. 4b). Subsequently, the stretching of the major axis of the ellipse results in a migration of the mean vorticity toward the positive lobes. The linear growth is maintained until enough vorticity has migrated toward the positive perturbation lobes, that the symmetry of the perturbations is lost due to non-linear interactions with the mean flow. (Figure 3c shows a representative instant, at which the '2' mode symmetry is clearly destroyed). The orientation of the axial vorticity is such that the negative perturbation lobes are distorted and drawn toward the center of the positive lobes. At this stage, and for the rest of the evolution (Figs. 3 c-f and 4 c-f), most of the vorticity is contained in twin helical vortex structures. As these structures migrate to a larger radius, differential rotation results in a peculiar orientation of features around the helical structures. Since differential rotation tends to align radial vorticity into azimuthally-oriented vorticity, a structure that is primarily oriented in the azimuthal direction is observed (most evident in Figs. 4 e,f) in the periphery of the core region. The structure of this region is schematized in Fig. 5 (a right handed coordinate system is used). Two distinct layers are present: the outermost layer (light iso-surface) is of a $+ve\ \omega_\theta$ and $-ve\ \omega_x$ orientation. The inner layer (dark iso-surface) is of $-ve\ \omega_\theta$ and $+ve\ \omega_x$. This *dipole vortex layer* emerges during the saturation phase and is convected radially outward during the decay phase (Figs. 3,4).

The presence of the mean negative ω_x near the edge of the core corresponds to a circulation overshoot (Fig. 6a). The presence of a local positive peak of ω_θ, while exaggerated in Fig. 7b can also be seen in Fig. 6c. At the latest investigated time for Case E, similar to the findings in [13], the secondary vortical structures are convected away from the core and an apparently

stable system composed of two helical lobes is observed. In Case I however, the breakdown of the dominant helical structures appear to drive the system toward a stable high-q Batchelor vortex configuration.

3.2 Turbulent Evolution

The evolution in the turbulent case is qualitatively similar to Case E, in that the helical modes are excited, core vorticity is concentrated in helical lobes and the *dipole* vortex layer is present at the periphery of the core. However, there are two distinct differences : (i) A multitude of helical instability modes are excited although most of the energy is concentrated in the most unstable normal mode, and, (ii) the dipole vortex layer breaks down into a multitude of distinct hairpin-type vortex structures. The origin of the hairpin structures is shown in Fig. 8: The dipole layer (Fig. 8a) has a structure similar to that shown in Fig. 5. However, secondary instabilities cause this layer to 'peel off' into hairpin vortices (Figs. 8 b,c) with a distinct structure (Fig. 9). The two legs of the hairpin are oriented such that the leg of the hairpin with a larger x coordinate is of negative ω_θ, whereas the other leg is of positive ω_θ and the head of the hairpin corresponds to a negative ω_x. Also, the head of the hairpin is at a larger radius than the legs, and hence, the associated negative ω_x contributes to the mean negative mean ω_x at that radial location. Self-induction causes the hairpin to convect radially outward. However, differential rotation tends to align it in the azimuthal direction - as the head of the hairpin rotates at a slower rate than the tail because of its relative radial location. The associated stretching intensifies ω_θ, resulting in a generation of significant enstrophy in an annular region around the core. Ultimately, the hairpin structures breakdown into elongated vortices (Figs. 2, 8d). During the decay phase, these structures move radially outward as the core vorticity tends toward a stable state. Throughout the simulation, at least 3-5 mesh points were guaranteed across the core diameter of the hairpin structure. The energy and enstrophy spectra were monitored such that there was no significant pile up of modes in the dissipation range. In the following section, the presence and signature of these structures will be explained from dynamic considerations. It has to be mentioned that while the presence of a circulation overshoot implies that the flow is centrifugally unstable, the instabilities are not sustained in the flow, and are instead convected radially outward.

4 Conserved quantities

For mean axisymmetric flow that is homogeneous in the axial directions, it can be shown that,

$$\frac{\partial}{\partial t}\left[\int_0^R r^2 v_\theta dr\right] = -[r^2\overline{v_r' v_\theta'}]_{r=R} - \nu\frac{\Gamma_o}{\pi}, \quad and, \tag{4}$$

$$\frac{\partial}{\partial t}\left[\int_0^R r v_x dr\right] = -[r\overline{v_r' v_x'}]_{r=R} \tag{5}$$

These relations are derived by integrating the angular and axial momentum equations over the radius. The former of the these relations is well known, for instance, eqn. 9 in [20]. In the present computations, it was confirmed that $\overline{r^2 v_r' v_\theta'}$ and $\overline{r v_r' v_x'}$ were both very small at large radii, and hence, total axial momentum is conserved and the total angular momentum depends only on the viscosity (and decays very slowly at large Reynolds numbers).

Presently, decomposing the instantaneous velocity field $\{v_x, v_r, v_\theta\}$ into a laminar solution (denoted by subscript l, which corresponds to the temporal evolution of the unperturbed Batchelor vortex) at that instant and a perturbation 'δ' (with $\{u, v, w\}$ being the deviation of the axial, radial and tangential velocity components, respectively, from the laminar solution),

$$\{v_x, v_r, v_\theta\}(x, r, \theta, t) = \{v_{x,l}, 0, v_{\theta,l}\}(r, t) + \{u, v, w\}(x, r, \theta, t), \tag{6}$$

the following relations can be derived:

$$\frac{\partial}{\partial t}\left[\int_0^R r^2 \widetilde{w} dr\right] = \left[-r^2\widetilde{vw} + \nu r^3 \frac{\partial}{\partial r}\left(\frac{\widetilde{w}}{r}\right)\right]_{r=R} \tag{7}$$

and,

$$\frac{\partial}{\partial t}\left[\int_0^R r\widetilde{u} dr\right] = \left[-r\widetilde{uv} + \nu r\frac{\partial \widetilde{u}}{\partial r}\right]_{r=R}, \tag{8}$$

where, $\widetilde{a} = \int_0^{2\pi} a d\theta$. It was confirmed from the simulations that at for sufficiently large R (few times r_{co}), the right hand sides of the above equations are negligible (less than 0.002% of maximum of the left hand side integrand), and therefore, the 'δ' angular and axial momentum flux are conserved, and *do not appear to depend on the viscosity*. These relations are significant because they can be used to study the transport of momentum in the flow field. Figure 10 shows the evolution of the aforementioned quantities (the LHS integrands) during the decay process. Clearly, there is a net loss of momentum (relative to the laminar evolution) inside the core and this is transferred to the exterior. It has to be recognized that the turbulent transport of mean angular and axial momentum is solely dependent on the terms $-\frac{\partial}{\partial r} r^2 \overline{v_r' v_\theta'}$ and $-\frac{\partial}{\partial r} r\overline{v_r' v_x'}$, respectively.

The 'δ' angular momentum can be expressed as

$$r^2\widetilde{w}(r) = r\int_0^r (\widetilde{\omega}_x - \omega_{x,l})rdr, \tag{9}$$

Then if $\widetilde{\omega}_x(r) > \omega_{x,l}(r) + \epsilon_x$ (a very plausible situation considering the fact that mean ω_x has convected to a larger radii from the axis) at some $r = r_1$, then, $\widetilde{\omega}_x(r) < \omega_{x,l}(r)$ at some $r = r_2 > r_1$. ($\epsilon_x > 0$ is related to the initial perturbation angular momentum). This is because the net 'δ' angular momentum has to be conserved and also due to the consistency condition at $r = 0$ as well as the compactness of $\widetilde{w}$. Evidence of this can be seen from Fig. 7a, in which, at the earliest shown instant, a sudden drop in ω_x (to a value below $\omega_{x,l}$) is observed near the edge of the vortical region. At later instances, the corresponding $\omega_{x,l} = 0$ (because laminar diffusion is much slower) and hence ω_x has to drop to negative levels to satisfy conservation.

Similarly, conservation of the axial momentum flux implies that if $\widetilde{v}_x(r) < v_{x,l}(r) - \epsilon_\theta$ (again, a possible situation because axial velocity decays at a higher rate than the laminar case) at some $r = r_1$, then, $\widetilde{v}_x(r) > v_{x,l}(r)$ at some $r = r_2 > r_1$. During the decay phase, since the peak axial velocity in the core is likely to be at smaller levels (relative to the laminar case) and the core radius is larger, the deficient momentum is likely to be regained outside the core. The requirement of compactness then assures $v_x = 0$ at some radius, resulting in a positive $\omega_\theta = -\partial v_x/\partial r$. This can be seen in Fig. 6c and Fig. 7b.

5 Reynolds stress evolution

During the linear growth stage, all the components of the Reynolds stress are concentrated in annuli, primarily inside the core. $\overline{v_r'^2}$ and $\overline{v_x'^2}$ peak at $0.6r_c(t)$ while $\overline{v_\theta'^2}$ peaks around $0.3r_c(t)$. Similar observations have been previously reported for a vortex with $q = 1.0$ in [11], in which a detailed analysis of the Reynolds stress budgets is also presented. (The transport equations for the Reynolds stresses in tensor form are given in Appendix C). During saturation and decay, these peaks move toward the vortex axis. As has been previously reported[21], $\overline{v_r'^2} > \overline{v_\theta'^2}$ because the primary production terms are of opposite sign. While the respective production terms of the Reynolds normal stresses peak away from the axis and dominate during the growth phase, the pressure (strain and transport) and turbulent transport terms appear to be highly significant during saturation and decay and are more active near the vortex axis. As a result, the normal stresses are concentrated near the axis during decay. In the potential part of the flow, the Corrsin-Kistler relation [22] $\overline{v_r'^2} = \overline{v_x'^2} + \overline{v_\theta'^2}$ is approximately satisfied.

The primary Reynolds shear stress components, $\overline{v_r' v_\theta'}$ and $\overline{v_x' v_r'}$ initially peak around a radius $0.6 r_c(t)$, but continue to migrate in a radially outward direction during the growth phase. The primary production terms in the Reynolds stress transport equations are, respectively: $P_{r\theta} = -s_{r\theta}(\overline{v_r'^2} + \overline{v_\theta'^2})$ and $P_{xr} = \omega_\theta(\overline{v_x'^2} + \overline{v_r'^2})/2$. (Note: $-s_{r\theta} = -(\partial v_\theta/\partial r - v_\theta/r)/2$ and ω_θ are primarily positive.) During the growth phase, the production terms are clearly dominant and dependent on the Reynolds normal stresses. During the decay phase as seen in Fig. 11a, $P_{r\theta}$ decays rapidly inside the core and relatively slowly outside it (in fact, there is some growth). It was also confirmed that the turbulent transport and pressure terms were not significant outside the core. Therefore, the peak $\overline{v_r' v_\theta'}$ migrates outside the core (Fig. 11c), coinciding with the location of the radially advecting vortex layer discussed in the previous section.

In contrast to $P_{r\theta}$, P_{xr} is primarily concentrated inside the core. This is because the former depends on the mean strain rate (which extends to $r \to \infty$), whereas the latter depends on the vorticity (which is mainly concentrated within $r < r_c(t)$). Accordingly, while the budget of $\overline{v_r' v_\theta'}$ outside the core is dominated by the production terms, the radial outward spread of $\overline{v_x' v_r'}$ is additionally dictated by the pressure and turbulent transport terms. Since the vorticity and Reynolds normal stresses are significant inside the core, P_{xr} is dominant inside the core, and hence, there is some generation of $\overline{v_x' v_r'}$ near the axis. It was also observed that, in general, the contribution of the turbulent transport terms is larger in the Reynolds normal stress budgets than in the shear stress budgets.

It appears that the elongated fine scale vortices are more efficient in generating $\overline{v_r' v_\theta'}$ correlation than a $\overline{v_x' v_r'}$. Thus, angular momentum transport to the exterior is more efficient.

6 Generation of $\overline{v_r' v_\theta'}$

As mentioned earlier, efficient transport of angular momentum is governed by the generation and transport of $\overline{v_r' v_\theta'}$. In this section, the associated physical mechanisms are sought. For a qualitative picture, consider Fig. 12a. The prominent vortical features are the two positive ω_x and the two negative ω_x structures. If only the positive ω_x structures were present, four $v_r' v_\theta'$ lobes (around each ω_x structure) of alternating sign will be generated. The presence of the additional dipole layer (distinguished by negative axial vorticity) results in an induced velocity field that generates positive $v_r' v_\theta'$, mainly outside the core. A similar mechanism appears to be in play in Case I (Fig. 12b), where toward the bottom left corner, the presence of the dipole layer surrounding the mean positive ω_x generates a local positive correlation of $v_r' v_\theta'$. Also

note that the presence of a secondary counter-rotating structure will result in an additional strain-rate, thus strengthening $P_{r\theta}$.

7 Summary

A range of issues related to the temporal evolution of an initially unstable turbulent Batchelor vortex were addressed. Considerable qualitative insight on the flow was obtained by studying the non-linear evolution of a single instability mode. The formation of a *dipole vortex layer* was shown to be critical to the evolution process. In the case of the turbulent vortex, the dipole layer breaks down into distinct hairpin structures, which are ultimately seen to degenerate into elongated fine scale vortices due to the action of straining caused by differential rotation. This results in the generation of the $r - \theta$ Reynolds stress in an annular region surrounding the core. The radially outward advection of these structures plays a key role in the transport of angular momentum to the external flow and the restabilization of the vortex. The transverse length scale of these structures is approximately $10 - 20\%$ of the inital core radius. Since these structures are dynamically important, care should be taken to resolve them if Large Eddy Simulations are attempted. The deviation of the mean angular and axial momentum from the laminar solution was shown to be compact and conserved and this was seen to dictate the characteristic signature of the dipole layer.

Appendix

A. Initial condition - Case I

The flowfield is initialized with an isotropic random-phase energy spectrum of the form $E(k) \approx k^2 e^{-k^2}$. Periodic boundary conditions are imposed and the flow was evolved until the skewness and flatness reached steady values. The resulting flow-field quantities were then multiplied by the function $r^n e^{-r^2}$, where $n = 0, 1, 2$ were experimented with. Finally, the mean vorticity was superposed on this flow. As mentioned in the paper, the flow evolution was found to be qualitatively insensitive to the initial condition as long as the initial turbulence kinetic energy was $< 2\%$ of the mean kinetic energy.

B. Initial condition - Case E

For case Case E, the $q = 0.5$ Batchelor vortex was superimposed with the most unstable eigenfunction corresponding to the axial wavenumber $k = 1$ and azimuthal wave number $m = -2$. A spectral collocation code was used to generate the Eigenfunction. The kinetic energy of the perturbation was set to 1×10^{-6} times that of the total kinetic energy. The growth rate from linear stability analysis (non-dimensionalized by the peak axial velocity deficit and initial core-radius) is $\omega_i = 0.260805$. As seen from Fig. 13, the initial growth rate from the computation matches the theoretical prediction, but non-linear effects appear to rapidly limit this value.

C. Reynolds stress budgets

As reported in Qin [11], the various terms in the Reynolds stress transport equations can be written in the following from:

$$\begin{aligned}
\frac{\partial}{\partial t}(\overline{v_i' v_j'}) &= \left[-V_k(\overline{v_i' v_j'})_{,k}\right] + \left[-\frac{1}{2}(\overline{v_i' v_k'}(V_{k,j} + V_{j,k}) + \overline{v_j' v_k'}(V_{k,i} + V_{i,k}))\right] \\
&+ \left[\frac{1}{2}(\overline{v_i' v_k'}(V_{k,j} - V_{j,k}) + \overline{v_j' v_k'}(V_{k,i} - V_{i,k}))\right] + \left[\overline{p'(v_{i,j}' + v_{j,i}')}/\rho\right] \\
&+ \left[-(\overline{v_i' v_j' v_k'})_{,k}\right] + \left[-(\overline{p' v_j'}\delta_{ik} + \overline{p' v_i'}\delta_{jk})_{,k}\right] + \left[\nu(\overline{v_i' v_j'})_{,kk}\right] + \left[2\nu(\overline{v_{i,k}' v_{j,k}'})\right]
\end{aligned}$$

where, the terms in the square brackets represent convection, production, rotation, pressure strain, turbulent transport, pressure transport, viscous diffusion and dissipation, respectively. Note: the subscript $()_{,k}$ represents a partial derivative.

References

[1] M. Lessen, P. Singh, and F. Paillet, "The stability of a trailing line vortex. Part 1. Inviscid theory," Journal of Fluid Mechanics, **63**, 753 (1974).

[2] E. Mayer, and K. Powell, "Viscous and inviscid instabilities of a trailing line vortex," Journal of Fluid Mechanics, **245**, 91 (1992).

[3] K. Stewartson, and S. Brown, "Near-neutral centre-modes as inviscid perturbations to a trailing line vortex," Journal of Fluid Mechanics, **156**, 387 (1985).

[4] C. Heaton, "Centre modes in inviscid swirling flows and their application to the stability of the Batchelor vortex," Journal of Fluid Mechanics, **576**, 325 (2007).

[5] D. Fabre, and L. Jacquin, "Viscous instabilities in trailing vortices at large swirl numbers," Journal of Fluid Mechanics, **500**, 239 (2004).

[6] C. Heaton, and N. Peake, "Transient growth in vortices with axial flow," Journal of Fluid Mechanics, **587**, 271 (2007).

[7] D. Pradeep, and F. Hussain, "Transient growth of perturbations in a vortex column," Journal of Fluid Mechanics, **550**, 251 (2006).

[8] C. Olendraru, A. Sellier, M. Rossi, and P. Huerre, "Inviscid instability of the Batchelor vortex: Absolute-convective transition and spatial branches," Physics of Fluids, **11**, 1805 (1999).

[9] L. Parras, and R. Fernandez-Feria, "Spatial stability and the onset of absolute instability of Batchelors vortex for high swirl numbers," Journal of Fluid Mechanics, **583**, 27 (2007).

[10] S. Ragab, and M. Sreedhar, "Numerical simulation of vortices with axial velocity deficits," Physics of Fluids **7**, 549 (1995).

[11] J. Qin, "Numerical simulations of a turbulent axial vortex," Ph.D. Dissertation, Purdue University, (1998).

[12] C. Pantano, and L. Jacquin, "Differential rotation effects within a turbulent Batchelor vortex," Direct and Large-Eddy simulation IV, (ERCOFTAC Series, Vol. 8), Lavoisier, (2002).

[13] I. Delbende, and M. Rossi, "Nonlinear evolution of a swirling jet instability," Physics of Fluids, **17**, 044103 (2005).

[14] J. Marshall, and M. Beninati, "External turbulence interaction with a columnar vortex," Journal of Fluid Mechanics, **540**, 221 (2005).

[15] Rayleigh, J., "On the dynamics of revolving fluids," Proceedings of the Royal Society of London Series A," **93**, 148 (1916).

[16] D. Pradeep, and F. Hussain, "Effects of boundary condition in the numerical simulations of vortex dynamics," Journal of Fluid Mechanics, **516**, 115 (2004).

[17] S. Rennich, and S. Lele, "Numerical method for incompressible vortical flows with two unbounded directions," Journal of Computational Physics, **137 (1)** 101 (1997).

[18] K. Duraisamy, and S. Lele, "DNS of temporal evolution of isolated vortices," Proceedings of the Center for Turbulence Research Summer Program, Stanford University, 2006.

[19] M. Melander, and F. Hussain, "Coupling between a coherent structure and fine-scale turbulence," Physical Review E, **48**, 2669 (1993).

[20] S. Govindaraju, and P. Saffman, "Flow in a turbulent trailing vortex," Physics of Fluids, **14**, 2074 (1971).

[21] J. Chow, G. Zilliac, and P. Bradshaw, "Mean and turbulence measurements in the near field of a wingtip vortex," AIAA Journal, **35 (10)**, 491 (1997).

[22] S. Corrsin, and A. Kistler, "Free-stream boundaries of turbulent flows," NACA Technical Note TN 3133, (1954).

List of Figures

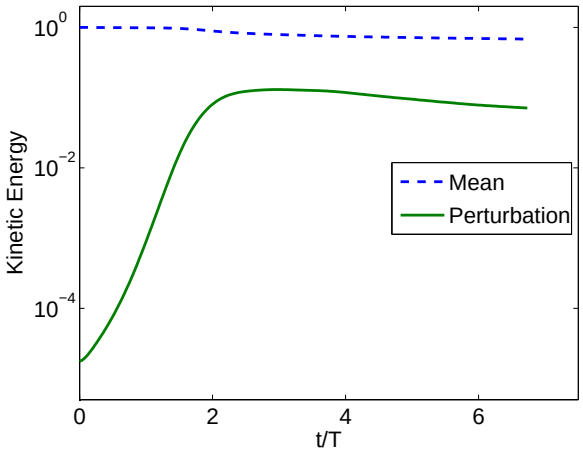

(a) Mean and Turbulent kinetic energy

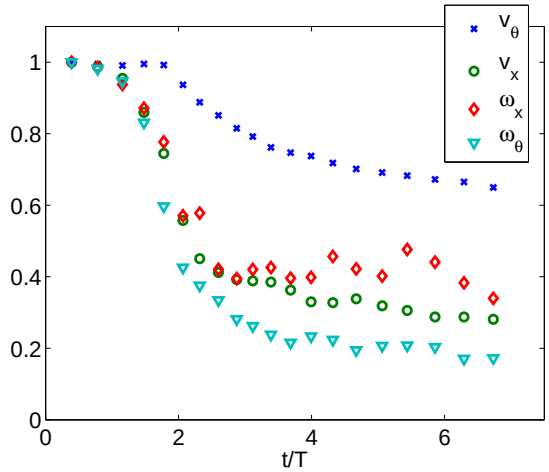

(b) Peak mean flow quantities

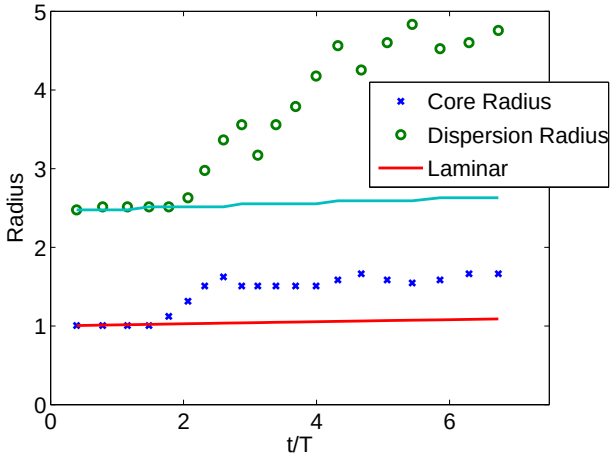

(c) Radial measures

Figure 1: Evolution of global quantities for Case I

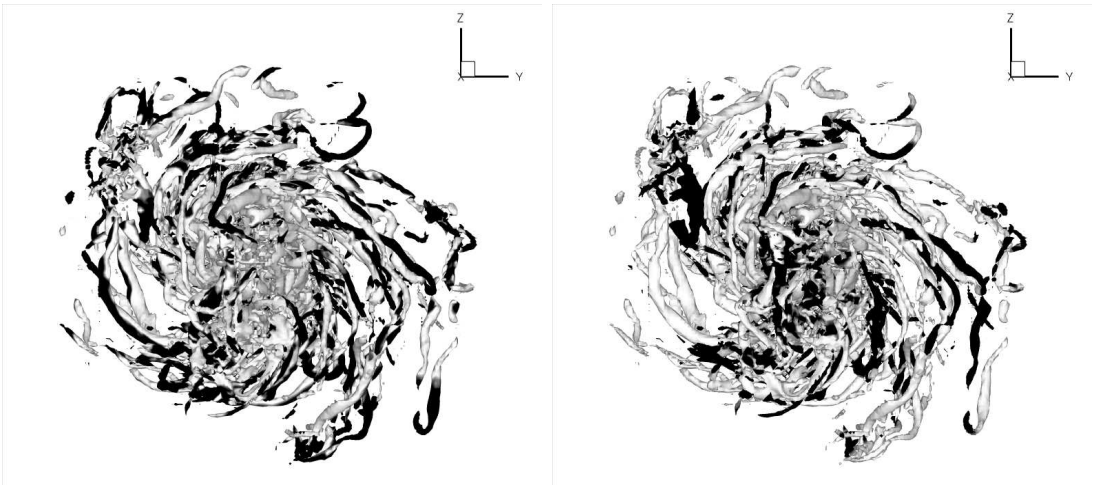

(a) ω_x (b) ω_θ

Figure 2: $|\boldsymbol{\omega}|$ iso-surfaces shaded with axial and azimuthal vorticity contours for Case I at $t/T = 3.4$. Light/Dark surface: $+ve/-ve$.

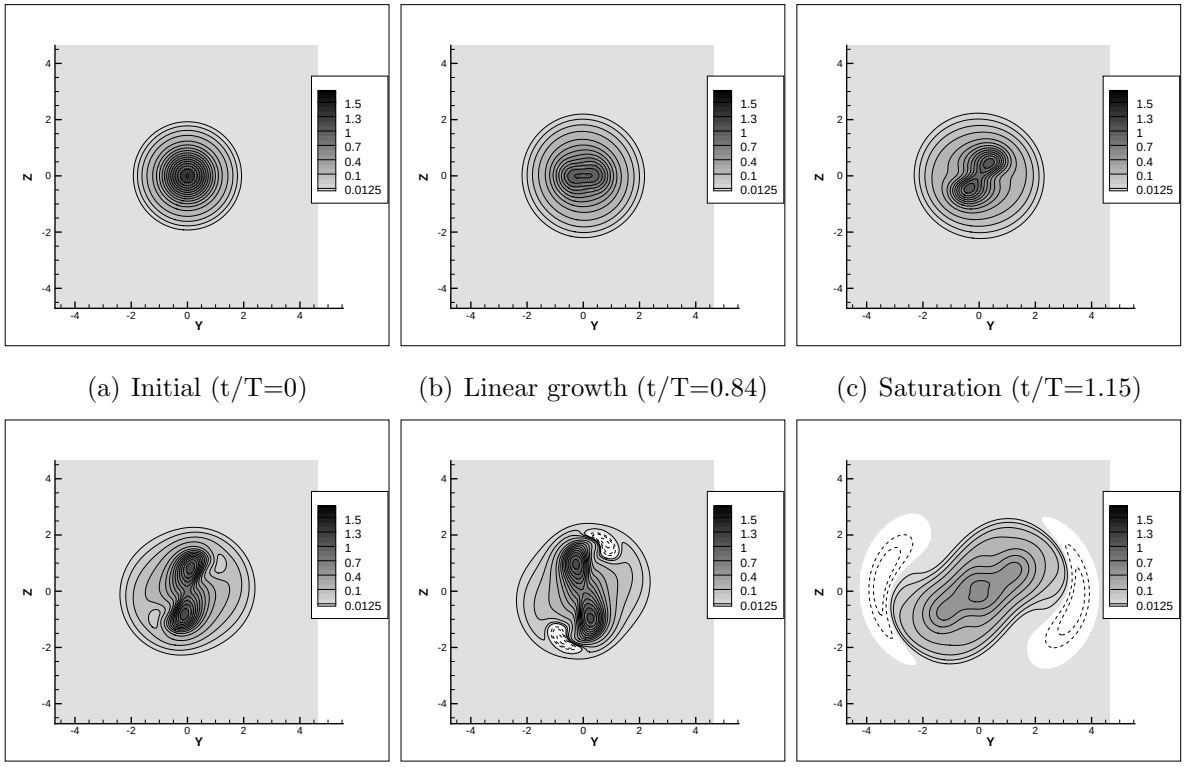

(a) Initial (t/T=0) (b) Linear growth (t/T=0.84) (c) Saturation (t/T=1.15)

(d) Saturation (t/T=1.47) (e) Decay (t/T=1.67) (f) Decay (t/T=3.02)

Figure 3: Axial vorticity contours for Case E. Negative vorticity shown as white patch / dashed lines

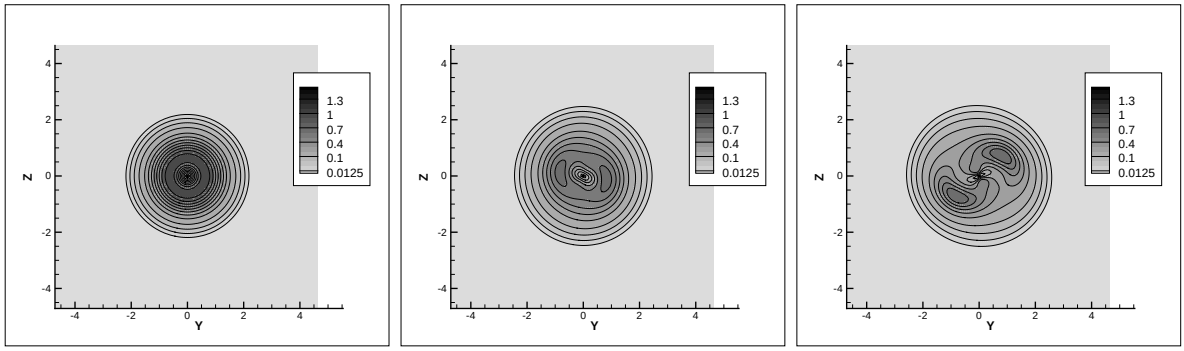

(a) Initial condition (t/T=0) (b) Linear growth (t/T=0.84) (c) Saturation (t/T=1.15)

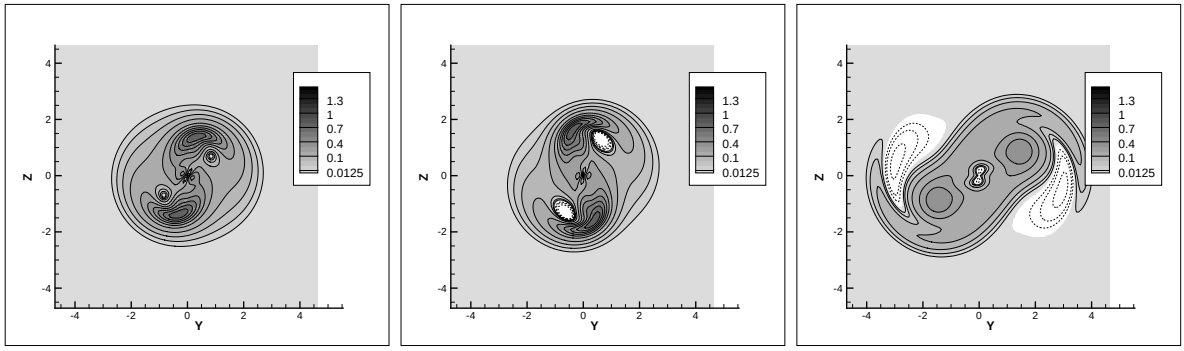

(d) Saturation (t/T=1.47) (e) Decay (t/T=1.67) (f) Decay (t/T=3.02)

Figure 4: Azimuthal vorticity contours for Case E. Negative vorticity shown as white patch / dashed lines

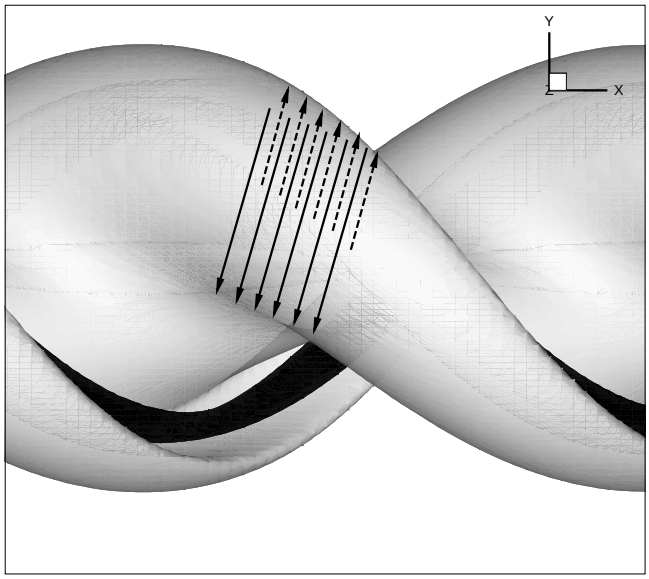

Figure 5: Case E (Saturation): ω_θ iso-surfaces (light/dark shade $+ve/-ve$. Also shown is a schematic of vortex lines (dashed lines are at a smaller radius compared to solid lines).

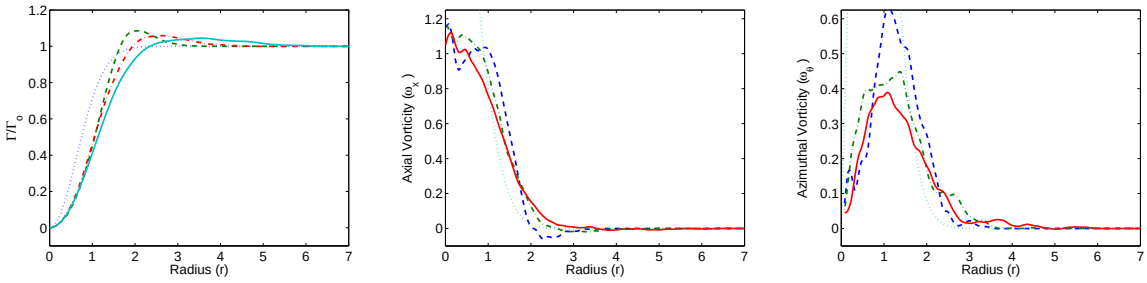

(a) Circulation (b) Axial vorticity (c) Azimuthal vorticity

Figure 6: Evolution of mean quantities for Case I. Dashes: $t/T = 2.6$, Dash-Dot: $t/T = 3.4$, Solid: $t/T = 5$. Initial condition also shown

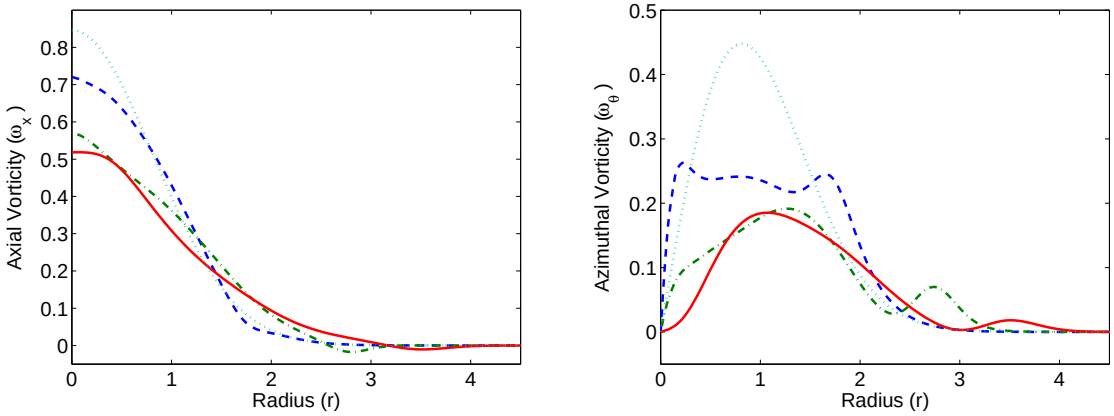

(a) ω_x (b) ω_t

Figure 7: Evolution for Case E during the decay phase. Dashed line is earliest shown instant and Solid line is latest. Laminar solution corresponding to earliest instant also shown

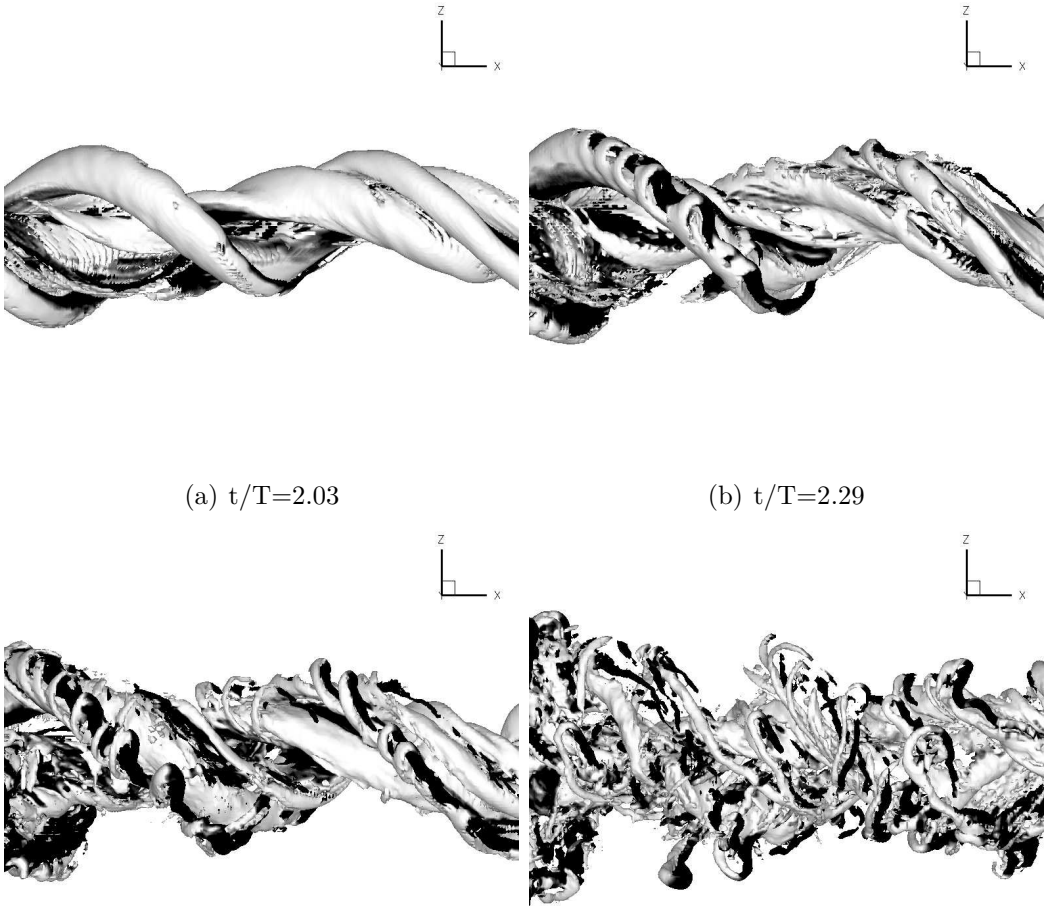

(a) t/T=2.03 (b) t/T=2.29

(c) t/T=2.57 (d) t/T=3.09

Figure 8: Case I: $|\boldsymbol{\omega}|$ iso-surfaces superposed with ω_θ contours. Dark shade corresponds to negative ω_θ.

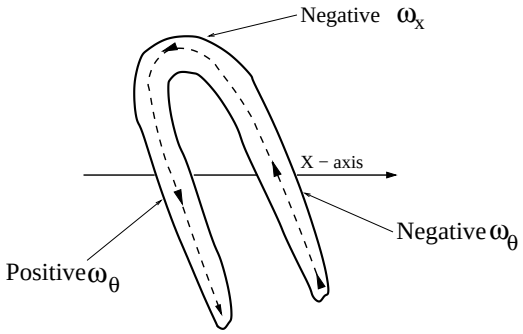

Figure 9: Schematic of hairpin structure. Dashed lines depict axis of local vorticity vector

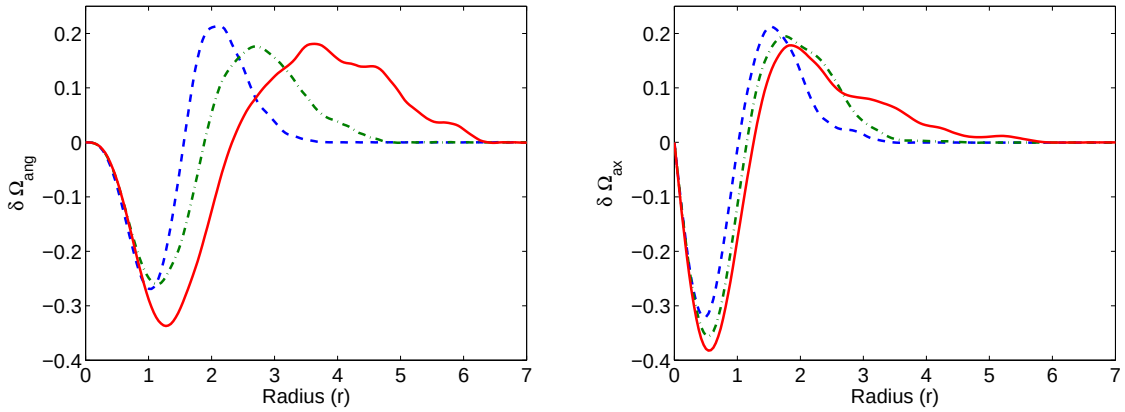

(a) $r\widetilde{rw}$ Ang. Mom. (b) $r\widetilde{u}$ Ax. Mom.

Figure 10: Evolution of 'δ' quantities for Case I. Dashes: $t/T = 2.6$, Dash-Dot: $t/T = 3.4$, Solid: $t/T = 5$

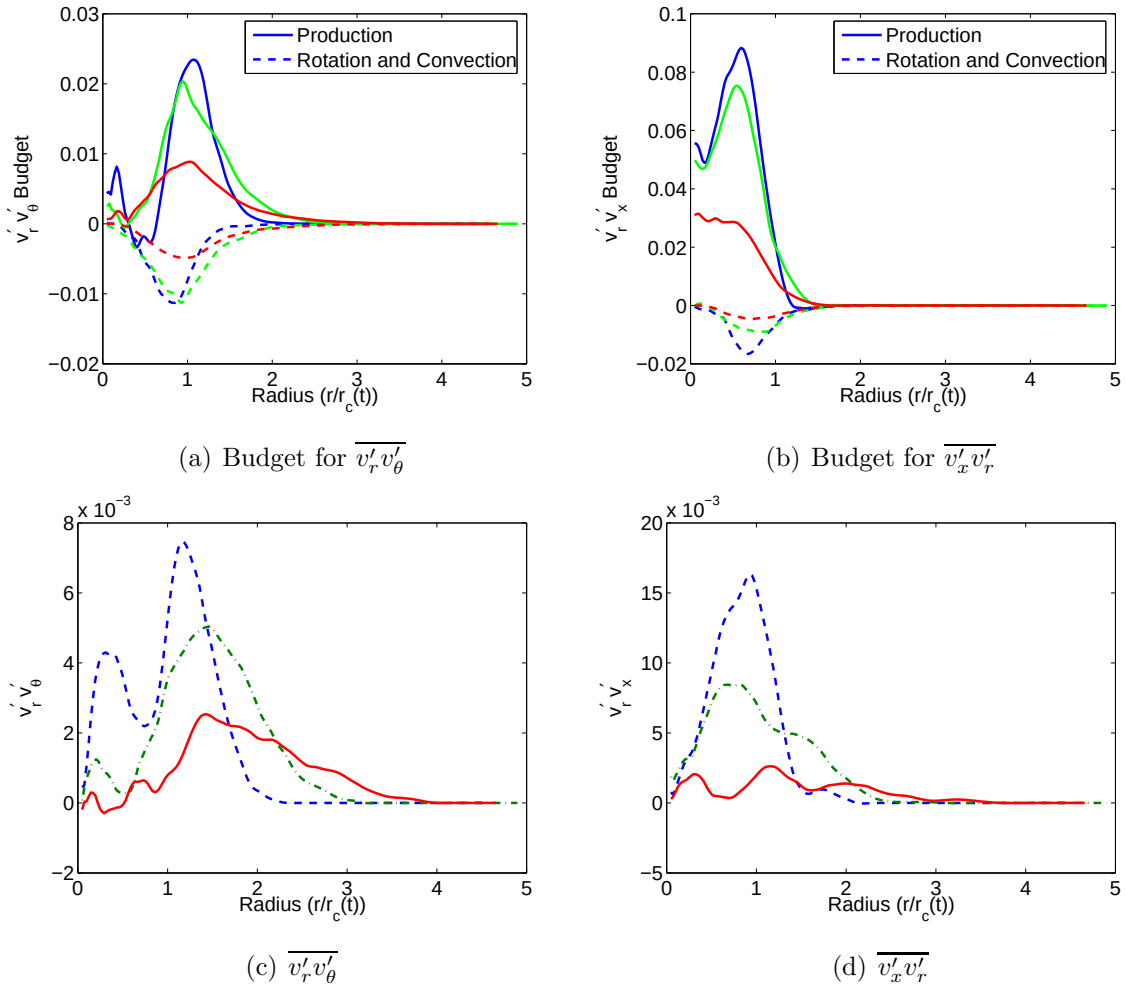

(a) Budget for $\overline{v_r' v_\theta'}$

(b) Budget for $\overline{v_x' v_r'}$

(c) $\overline{v_r' v_\theta'}$

(d) $\overline{v_x' v_r'}$

Figure 11: Reynolds stress and some budgets for Case I at times $t/T = \{2.6, 3.4, 5\}$, with increasing time corresponding to decreasing peak production

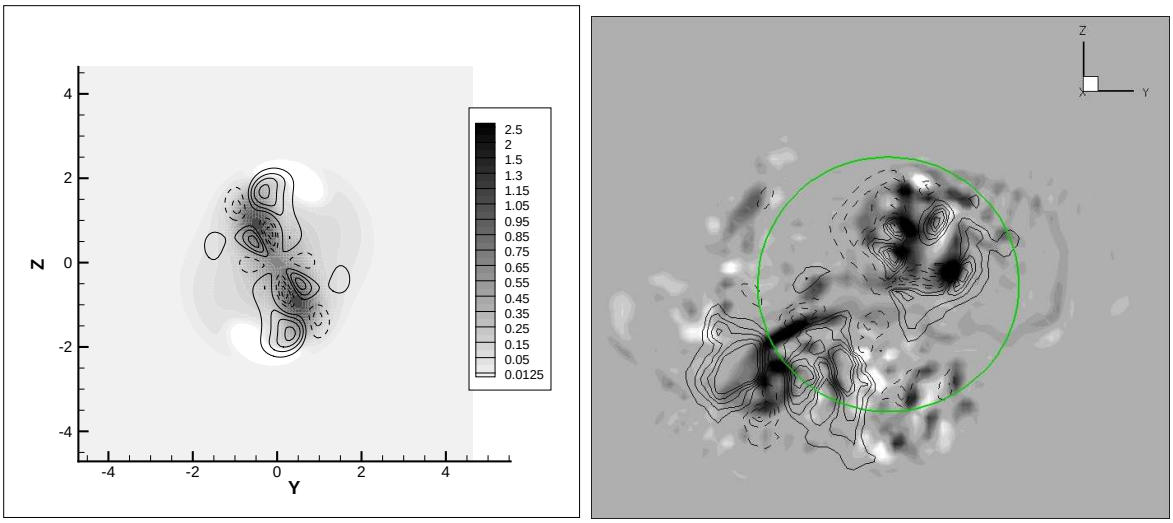

(a) Case E, Saturation phase

(b) Case I, $t/T = 3.4$

Figure 12: Representative instantaneous streamwise sections during the decay phase. Contours of ω_x and lines of $v_r' v_\theta'$ shown. Negative ω_x shaded dark, Negative $v_r' v_\theta'$ shown in dashed lines

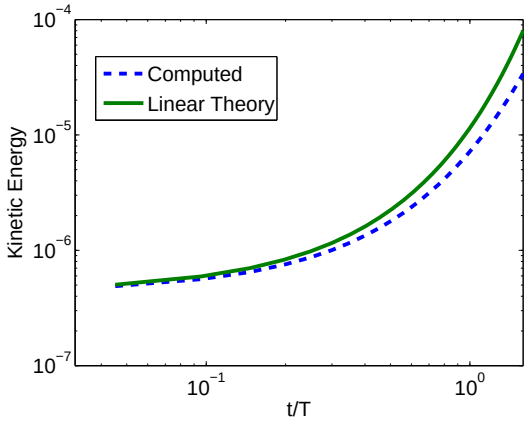

Figure 13: Comparison of growth rate of kinetic energy in the $k = 1$ axial mode for Case E